

Enhanced Ferroelectric Polarization in Epitaxial $\text{BiFeO}_3\text{-}\text{BiMg}_{2/3}\text{Nb}_{1/3}\text{O}_3$ Films

Yajie Han[✉], Zhijie Liu, Zhiyu Liu, Hongying Chen, Pengxiang Hou, Jiayi Li[✉], Yuqi Wang, Yu Deng, Yurong Yang,^{*} and Di Wu^{✉†}

National Laboratory of Solid State Microstructures, College of Engineering and Applied Sciences, Jiangsu Key Laboratory of Artificial Functional Materials, Nanjing University, Nanjing 210023, People's Republic of China

(Received 16 December 2022; revised 6 April 2023; accepted 27 April 2023; published 19 May 2023)

Remanent polarization is a key parameter of a ferroelectric material. A large remanent polarization is favorable for various ferroelectric applications. Here, we report a large remanent polarization of $116.8 \mu\text{C cm}^{-2}$ observed in $\text{BiMg}_{2/3}\text{Nb}_{1/3}\text{O}_3$ (BMN)-modified BiFeO_3 (BFO) thin films, epitaxially deposited on (001)-oriented SrTiO_3 substrates buffered with $\text{La}_{2/3}\text{Sr}_{1/3}\text{MnO}_3$ electrodes. Combined experimental analyses and first-principles calculations reveal that the incorporation of 10 mol % BMN into BFO increases both the intrinsic and extrinsic contributions, resulting in doubled polarization. The intrinsic polarization calculated for BFO-BMN is larger than that of BFO due to enhanced ionic displacements. Compared with epitaxial BFO films in a rhombohedral structure with an interaxial angle of $\alpha = 89.72^\circ$ and quasitetragonal $c/a = 1.018$, the epitaxial BFO-BMN films become more tetragonal-like, with $\alpha = 89.91^\circ$ and $c/a = 1.037$. Moreover, a unique rotated twinning-domain structure is developed in the BFO-BMN thin films, further increasing the out-of-plane polarization by rotating the [111] direction toward the film's normal. These results provide additional opportunities to increase ferroelectric polarization through composition engineering.

DOI: 10.1103/PhysRevApplied.19.054064

I. INTRODUCTION

Ferroelectric materials exhibit a wide spectrum of physical properties in response to electrical, mechanical, thermal, and optical stimuli, making them attractive for applications in nonvolatile random-access memories, piezoelectric transducers and sensors, photovoltaic cells, etc. [1–7]. The remanent polarization (P_r), as a key ferroelectric parameter, lies in the core of various ferroelectric applications due to its strong coupling to various structural and functional parameters and external stimuli [2,8,9]. For this reason, a larger P_r is highly desired in most applications to achieve a stronger response. For example, ferroelectric thin films with a large polarization are able to store more charges [10], making it easier to distinguish the “0” and “1” states in ferroelectric random-access memories [11–13]. A large polarization also means stronger adsorption of polar molecules on the surface of ferroelectric particles, which is advantageous for achieving more effective catalysis [14,15].

BiFeO_3 (BFO) has been intensively studied as a well-known room-temperature single-phase multiferroic material [5,16–19]. In particular, the high spontaneous polarization ($P_s \sim 100 \mu\text{C cm}^{-2}$) of BFO makes it a promising candidate for memory applications [20,21]. Bulk BFO

has a rhombohedrally distorted perovskite structure in the $R3c$ space group with lattice parameter $a = 3.965 \text{ \AA}$ and interaxial angle $\alpha = 89.45^\circ$ [22]. The low symmetry of the rhombohedral cell allows four possible structural variants (r_1, r_2, r_3 , and r_4) with their spontaneous polarization along the $\langle 111 \rangle$ direction of the pseudocubic lattice, producing eight possible domain variants with different polarization directions ($P_1^+, P_1^-, P_2^+, P_2^-, P_3^+, P_3^-, P_4^+$, and P_4^-) [23], as schematically shown in Fig. 1. This gives rise to complicated domain patterns and additional opportunities to tailor P_r [24,25]. In the case of epitaxial BFO thin films, engineering of the strain [26,27], electrostatic boundary [28], and chemical composition [26,29,30] is used to manipulate polarization. The chemical-composition-engineering strategy, by doping ions or forming solid solutions, is widely accepted as a simple but effective way because it modulates physical properties drastically by changing the local lattice structure.

Bi-based perovskitelike compounds $\text{Bi}M'M''\text{O}_3$ ($M' = \text{Zn}^{2+}, \text{Mg}^{2+}, \dots$; $M'' = \text{Ti}^{4+}, \text{Nb}^{5+}, \dots$) are frequently used as a component to form solid solutions with a variety of ferroelectrics to promote crystallization quality and to enhance relaxor behaviors. These solid solutions include $\text{NaNbO}_3\text{-}\text{BiZn}_{1/2}\text{Ti}_{1/2}\text{O}_3$ [31], $\text{BaTiO}_3\text{-}\text{BiMg}_{1/2}\text{Zr}_{1/2}\text{O}_3$ [32], $\text{BaTiO}_3\text{-}\text{BiZn}_{2/3}\text{Nb}_{1/3}\text{O}_3$ [33], $\text{BaTiO}_3\text{-}\text{BiMg}_{2/3}\text{Nb}_{1/3}\text{O}_3$ [34], $\text{BFO-SrTiO}_3\text{-}\text{BiMg}_{2/3}\text{Nb}_{1/3}\text{O}_3$, etc [35]. However, the improvement of P_r in a $\text{Bi}M'M''\text{O}_3$ -modified ferroelectric is rare in the literature.

^{*}yangyr@nju.edu.cn

[†]diwu@nju.edu.cn

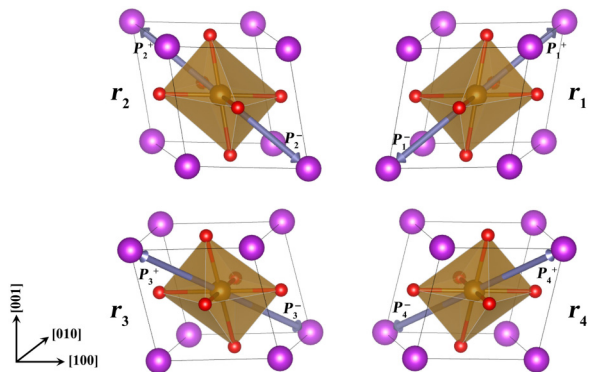


FIG. 1. Schematic illustration of the four structural variants (r_1 , r_2 , r_3 , and r_4) in rhombohedral BFO, where the arrows represent eight polarization directions along the $\langle 111 \rangle$ directions of the pseudocubic lattice.

Here, we report a large P_r of about $116.8 \mu\text{C cm}^{-2}$ in 10 mol% $\text{BiMg}_{2/3}\text{Nb}_{1/3}\text{O}_3$ -modified BFO (abbreviated hereafter as BFO-BMN) films, 540 nm in thickness, and deposited epitaxially on $\text{La}_{2/3}\text{Sr}_{1/3}\text{MnO}_3$ (LSMO)-buffered (001)-oriented SrTiO_3 (STO) substrates. The origin of this large polarization is investigated by x-ray diffraction (XRD), piezoelectric force microscopy (PFM), transmission electron microscope (TEM), and first-principles calculations.

II. EXPERIMENTAL METHODS

A. Film deposition

Both the BFO-BMN and BFO films are deposited on (001)-oriented STO single-crystalline substrates by pulsed-laser deposition, using a PLD20 KrF excimer laser ($\lambda = 248 \text{ nm}$, Excimer, China). Before deposition, commercially available STO substrates are treated in NH_4F -buffered HF solution for 45 s, followed by annealing in a flow of O_2 at 950°C for 75 min, to achieve a TiO_2 single-terminated surface. LSMO, BFO, and BFO-BMN thin films are all deposited under an oxygen pressure of 100 mTorr with a laser power density of 1.5 J cm^{-2} . The LSMO electrode is first deposited at 750°C with a pulse-repetition rate of 2 Hz. Then, the BFO or BFO-BMN films are deposited at 650°C with a pulse-repetition rate of 4 Hz on the LSMO electrode. LSMO, BFO, and BFO-BMN ceramic targets are prepared by conventional solid-state reaction. 5% excess Bi is added to BFO and BFO-BMN targets to compensate for Bi evaporation. Pt top electrodes, 50 μm in diameter, are deposited through a shadow mask at room temperature using an AJA Orion-8-UHV sputtering system.

B. Characterization

The composition of the deposited BFO-BMN film is analyzed by energy-dispersive x-ray spectroscopy (EDS)

coupled with a field-emission scanning electron microscope (SEM, Zeiss Ultra 55). XRD measurements are conducted with a Bruker D8 Discover high-resolution diffractometer. The surface morphologies are imaged using an Asylum Research Cypher-ES atomic force microscope (AFM). The in-plane and out-of-plane domain configurations are detected by PFM using the same AFM system. The cross-section TEM samples are prepared with a focused ion beam (Helios G4 UX, Thermo Fisher). The dark-field TEM images and the selected-area electron diffraction (SAED) patterns are recorded on an FEI TF20 microscope. The atomic resolution images and EDS element-mapping results are acquired using an aberration-corrected scanning transmission electron microscope (STEM) equipped with a high-angle annular-dark-field (HAADF) detector in an FEI Titan3 G2 60-300 microscope, operating at 300 kV. The polarization-electric field (P - E) hysteresis loops and leakage-current characteristics are measured using a standard ferroelectric tester (Precision Multiferroic, Radian Technologies).

C. First-principles calculations

The first-principles calculations are performed within density-functional theory using projector-augmented-wave (PAW) potentials, as implemented in the Vienna *ab initio* simulation package [36]. The generalized gradient approximation of the Perdew-Burke-Ernzerhof function is employed to describe the exchange-correlation interactions [37]. For the PAW potentials, Bi $6s^25d^{10}6p^3$, Mg $2s^2$, Nb $4s^24p^65s^14d^4$, Fe $4s^23d^6$, and O $2s^22p^4$ are treated as valence electrons. A plane-wave cutoff energy of 550 eV and $1 \times 1 \times 3$ k -point grid mesh are used for integrations within the Brillouin zone for the $4 \times 4 \times 2$ (160-atom) supercell. Total energies are converged within 10^{-7} eV for structural optimization until the residual force convergence on each atom is less than 1 meV \AA^{-1} . The VESTA package is used to display the crystal structure [38]. Spontaneous polarizations are calculated using Born effective charges and atom displacements relative to the corresponding centrosymmetric position with density-functional perturbation theory [39].

III. RESULTS AND DISCUSSION

A. Structural characterization

The EDS spectrum of the deposited BFO-BMN film shows a film composition of $\text{Bi:Fe:Mg:Nb} = 1:0.938:0.050:0.039$ (see Supplemental Material S1 [40]), in agreement with the nominal value. Figure 2(a) shows the XRD θ - 2θ pattern of the BFO-BMN film deposited on (001) LSMO/STO substrate. Only (00l) peaks from BFO-BMN, LSMO, and STO are observed, indicating the formation of a single-phase film. The (00l) peak positions of the BFO-BMN film yield an out-of-plane lattice constant, c ,

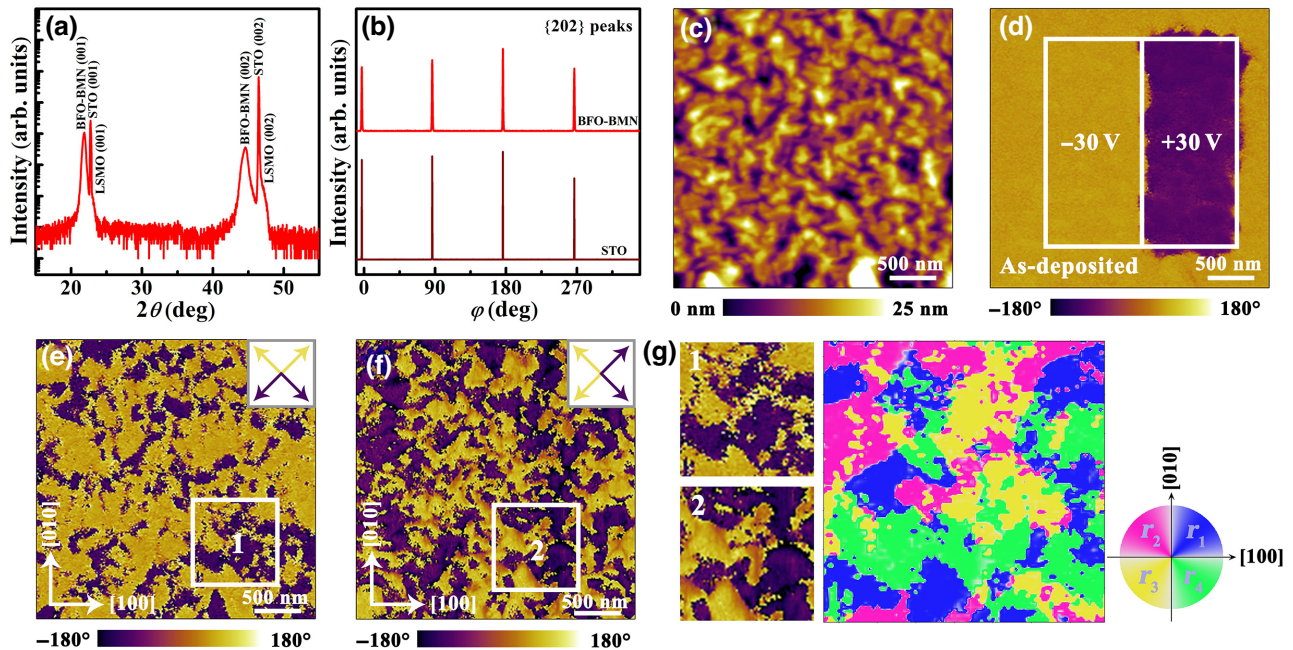


FIG. 2. (a) XRD θ - 2θ pattern of the BFO-BMN film deposited on (001) LSMO/STO; (b) φ scans of the {202} reflections of the BFO-BMN film and STO substrate; (c) AFM image of the BFO-BMN film surface; (d) out-of-plane PFM phase image, and in-plane PFM phase images measured with the cantilever aligned along (e) [100] and (f) [010] directions of the BFO-BMN film. Insets in (e),(f) show possible directions of polarization for both yellow and purple contrasts; (g) magnified images of in-plane PFM phases, and corresponding distribution of four structural variants for the regions marked with white squares in (e),(f).

of about 4.065 Å, which is larger than that of bulk BFO-BMN (3.968 Å) due to the compressive in-plane strain imposed by the substrate (see the Supplemental Material S2 [40]). XRD φ scans of the {202} reflections of both the BFO-BMN film and the STO substrate are performed to analyze the in-plane structural relationships, as shown in Fig. 2(b). The four peaks at 90° intervals in φ correspond to the fourfold symmetry of the (202) plane. The well-aligned {202} peaks of BFO-BMN and STO reveal a high-quality epitaxy. As checked by AFM, the BFO-BMN film surface exhibits a root-mean-square roughness of 5.23 nm over an arbitrarily selected 3×3 -μm² area, as shown in Fig. 2(c). After poling with -30 and $+30$ V on the left and right halves of the central 2×2 -μm² area, respectively, the out-of-plane PFM phase is imaged, as shown in Fig. 2(d). The two domains with 180° phase contrast indicate electric-field-induced polarization switching, which is a demonstration of the ferroelectric nature. The domains written on the BFO-BMN film remain stable for at least 24 h, indicating excellent polarization retention of BFO-BMN, which is better than that of the pure BFO film (see the Supplemental Material S3 [40]). The phase contrast of the as-deposited region is homogeneous and is the same as that of the negative-voltage-poled area, indicating that the out-of-plane polarization of the as-deposited BFO-BMN film is preferentially pointing upward. The in-plane PFM phase images of the as-deposited BFO-BMN

film are recorded with the cantilever aligned along the [100] and [010] directions, as shown in Figs. 2(e) and 2(f), respectively. Note that, for both yellow and purple contrasts, there are two possible directions of polarization, as shown in the insets. The results indicate that the in-plane polarization of the BFO-BMN film points to four different orientations [26]. Combining both out-of-plane and in-plane PFM images, all four structural variants, r_1-r_4 , can be identified in the BFO-BMN film with preferential polarization P_1^+ , P_2^+ , P_3^+ , and P_4^+ (Fig. 1). To be more explicit, Fig. 2(g) shows magnified in-plane PFM images of the areas marked with white squares in Figs. 2(e) and 2(f), and the corresponding distribution of these four structural variants is shown in the right panel.

Detailed structural information is collected from x-ray reciprocal-space-mapping (RSM) measurements. Figures 3(a) and 3(b) show the RSM measurements around the (002) reflections of STO for BFO-BMN/LSMO/STO heterostructures at two different in-plane orientations with $\varphi = 0^\circ$ and $\varphi = 45^\circ$, respectively, where φ denotes the angle between the [100] axis of STO and the projection of the incident x-ray beam on the (00l) plane of STO. At $\varphi = 0^\circ$, the (002) reflection of BFO-BMN shows a horizontal split into two peaks, as shown in Fig. 3(a), which can be attributed to the existence of two sets of (002) planes in the sample. The two peaks deviate slightly from $H = 0$, indicating that the (002) plane of the BFO-BMN film is

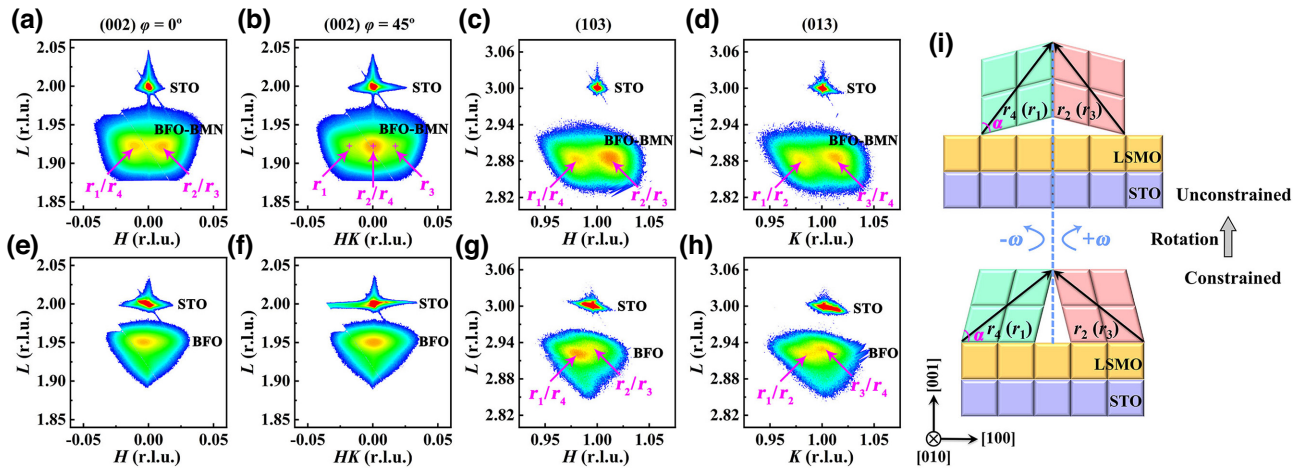


FIG. 3. RSM measurements around the (002) reflections of the STO substrate at $\varphi = 0^\circ$ and 45° , and RSM measurements around the (103) and (013) reflections, respectively, for (a)–(d) BFO-BMN and (e)–(h) BFO films. Reciprocal lattice unit (r.l.u.) is normalized to the STO substrate ($1 \text{ r.l.u.} = 2\pi/3.905 \text{ \AA}^{-1}$); (i) schematic illustration of rotation of the rhombohedral twinning structure for the epitaxial BFO-based films on LSMO/STO substrates. Black arrows in different structural variants show the polarization direction along (111).

not parallel to that of the STO substrate, but rotated oppositely with respect to the [100] direction at an angle of $\omega = \pm 0.33^\circ$. In contrast, the (002) reflection of the BFO-BMN film splits horizontally into three peaks at $\varphi = 45^\circ$, as shown in Fig. 3(b), suggesting that there are three sets of (002) planes observed from this direction. Referring to the structural variants of rhombohedral ferroelectrics proposed by Streiffer *et al.* (Fig. 1) [23], at $\varphi = 0^\circ$, the (002) plane of r_1 overlaps with that of r_4 , and the (002) plane of r_2 overlaps with that of r_3 , giving rise to the two (002) peaks observed in Fig. 3(a). At $\varphi = 45^\circ$, the (002) plane of r_2 overlaps with that of r_4 , parallel to the (001) plane of STO, whereas r_1 and r_3 are rotated oppositely with respect to the [110] direction at an angle of $\omega = \pm 0.52^\circ$, leading to three peaks, with the middle one having stronger intensity than the other two, as observed in Fig. 3(b). Therefore, there are four rotated twinning-domain variants in the BFO-BMN film, as proposed previously [23]. Figure 3(i) schematically shows these four rotated domain variants on the (001) LSMO/STO substrate, viewed along the [010] direction. The asymmetric (103), (013), ($\bar{1}03$), and ($\bar{0}\bar{1}3$) reflections of the BFO-BMN film also exhibit two peaks with almost the same L but different H and K values, as shown in Figs. 3(c) and 3(d) and Fig. S4 within the Supplemental Material [40]. Peak splitting in both (HOL) and (OKL) further confirms the coexistence of four rotated twinning domains, which typically occurs for epitaxial BFO-based films [41,42]. The splitting along the [100] and [010] directions also suggests the predominant 109° domains in the film [43,44].

As a reference, RSM measurements around the (002) and {103} reflections for the BFO film are shown in Figs. 3(e)–3(h) and Fig. S5 within the Supplemental

Material [40]. A broad reciprocal lattice point is observed for the (002) reflection at both $\varphi = 0^\circ$ and 45° , whereas slight splitting along H (K) and L directions is detected for all {103} diffraction peaks of BFO. The weak intensities of the structural variants indicate that the in-plane twinning structure is initiated, but the out-of-plane twinning rotation is not fully developed in the BFO film. A similar phenomenon for the formation and rotation of the twinning structure was reported previously. For example, Daumont *et al.* reported the structural evolution from a fully coherent lattice to a partially relaxed one with the formation of in-plane twins in BFO films on STO substrates as the film thickness increases from 12 to 18 nm [45]. Liu *et al.* studied a 720-nm-thick epitaxial BFO film deposited on SrRuO₃/STO, showing rhombohedral twins with out-of-plane twinning rotation [46]. Panchwanee *et al.* observed the rotated orthorhombic twins in the epitaxial SmFeO₃ film on the LaAlO₃ substrate [47]. Previous research pointed out that lattice rotations and modulations in epitaxial films could be induced by misfit strain [48]. During epitaxial deposition, lattice mismatch and symmetry mismatch results in normal strain and shear strain, respectively, causing a complex lattice-relaxation process as the elastic energy accumulates with increasing film thickness. The rotation of the twinning domain provides a possible way to alleviate the constraint of the underlying substrate and thereby partially relaxing the strain [49–51]. As schematically shown in Fig. 3(i), the twinning domains may be coherent with the substrate in the initial stage and the lattice rotates gradually to achieve an unconstrained configuration, reducing the elastic energy. By comparing the RSM measurements of the BFO-BMN and BFO films, the BFO film is closer to the constrained

structure coherent with the substrate lattice, while the BFO-BMN film is closer to the unconstrained one with rotated twins. A comparison of the (103) reflections for 60-nm-thick BFO-BMN and BFO films are shown in Fig. S6 within the Supplemental Material [40]. The thin BFO film exhibits only a single peak. However, horizontal peak splitting, demonstrating the rotated twinning domains, can still be observed clearly in the 60-nm-thick BFO-BMN film. These results suggest that the introduction of BMN into BFO facilitates the formation of rotated twinning domains.

Another effect of the incorporation of BMN into the BFO film is reflected by the changes in the crystal structure. From the RSM measurements shown in Fig. 3 and Figs. S4 and S5 within the Supplemental Material [40], the in-plane and out-of-plane lattice constants of the BFO-BMN film are calculated to be $a \approx b \approx 3.919 \text{ \AA}$ and $c \approx 4.065 \text{ \AA}$, resulting in a large tetragonality with $c/a = 1.037$. The lattice parameters correspond to a distorted rhombohedral cell with $\alpha = 89.91^\circ$. In contrast, the lattice constants of the BFO film can be extracted as $a \approx b \approx 3.935 \text{ \AA}$, $c \approx 4.004 \text{ \AA}$, and $\alpha = 89.72^\circ$, yielding a quasitetragonal c/a of 1.018. Bulk BFO is rhombohedral, with $\alpha = 89.45^\circ$ and pseudocubic $c/a = 1.000$ [22]. Epitaxial BFO-based films can be tetragonal-like due to

epitaxial strain from the substrates. For example, the BFO film deposited on SrRuO₃/STO is tetragonal-like, with $\alpha = 89.50^\circ$ and $c/a = 1.016$ [17]. This indicates that the BFO film lattice here is not fully relaxed to the bulk rhombohedral unit cell but is close to that of the reported tetragonal-like epitaxial film. The crystal structure of the BFO-BMN film is even closer to tetragonal than our BFO film and the reported BFO film deposited on SrRuO₃/STO [17]. It should be noted that the monoclinic phase is widely considered as a structural bridge at the rhombohedral-to-tetragonal transition. Distinguished by RSM measurements, the so-called “tetragonal-like” structure here is indeed a M_A -type monoclinic phase [30,52,53]. But for simplicity here, we focus on the structural comparison of BFO-BMN and BFO thin films. It can be concluded that the incorporation of BMN into the BFO film gives rise to a more tetragonal-like structure with an increased tetragonality, c/a , than that of the pure BFO film.

The domain structure of the BFO-BMN film is further verified by TEM. Figure 4(a) shows the cross-section dark-field TEM image of the BFO-BMN/LSMO/STO heterostructure recorded along the [010] zone axis of the STO substrate. Domains with bright and dark contrasts are separated by vertical (100)-type domain walls, indicating the

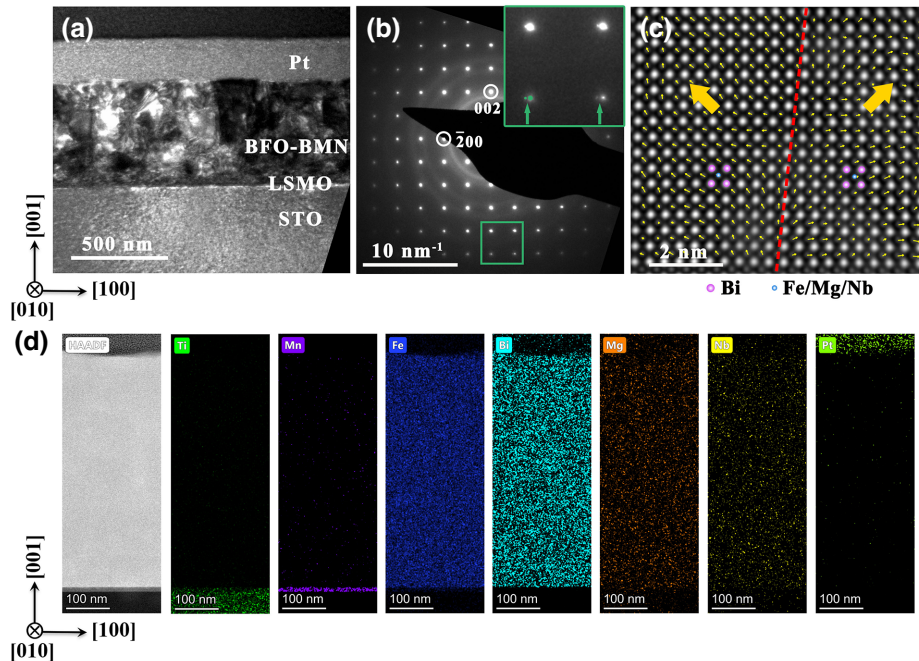


FIG. 4. (a) Cross-section dark-field TEM image of BFO-BMN/LSMO/STO heterostructure taken along the [010] zone axis of STO; (b) SAED pattern captured from a region including 109° domain walls close to the BFO-BMN film surface. Inset in the upper-right corner shows a magnified image of the diffraction spots indicated by the green square. Green arrows indicate splitting of the high-order diffraction spots; (c) HAAADF STEM image with a map of B -site-cation displacement vectors overlaid across a vertical domain boundary in the BFO-BMN film. Yellow arrows denote the displacement vectors of B -site Fe^{3+} , Mg^{2+} , or Nb^{5+} . Red dashed line indicates the 109° domain wall. Red and blue circles at both sides of the domain wall denote the Bi and Fe, Mg, or Nb columns, respectively; (d) cross-section HAADF STEM image of BFO-BMN/LSMO/STO and corresponding EDS mapping for Ti, Mn, Fe, Bi, Mg, Nb, and Pt.

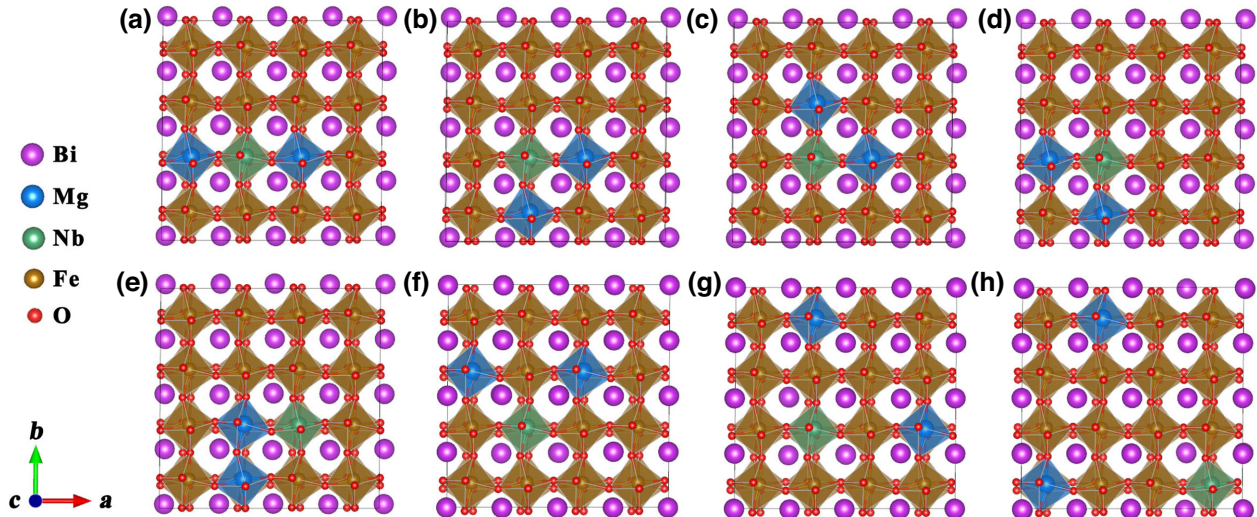


FIG. 5. (a)–(h) Possible atomic configurations of the BFO-BMN supercells viewed from the [001] direction.

existence of 109° domains in the film [43,44]. Figure 4(b) shows the SAED pattern captured from the region, including the vertical domain boundary. The diffraction ring is from the top Pt protective layer. The (001) and (100) planes have different spacings, with $d_{(001)}/d_{(100)} = 1.032$, which is comparable to the value of $c/a = 1.037$ obtained by XRD. The split along the [100] direction in the high-order diffraction spots, as indicated by green arrows in the magnified image in the inset of the SAED pattern, again reveals the presence of 109° domain walls. Figure 4(c) shows the atomically resolved HAADF STEM image with a superposition of *B*-site-cation displacement vectors, which is taken across a vertical domain boundary (red dashed line). Since the contrast of a HAADF STEM image is proportional to the atomic number of the columns by Z^2 , one can identify the atoms directly from the contrast. Here, the Bi columns appear as the brightest dots, and the Fe (Mg or Nb) columns show weaker contrast, as depicted by red and blue circles in the image. Based on the HAADF STEM image, the domain structure can be identified according to the displacement vectors of *B*-site Fe^{3+} (Mg^{2+} or Nb^{5+}) relative to the center of mass of the four-nearest *A*-site Bi^{3+} neighbors [54–56]. The yellow arrows denote the displacement vectors of *B*-site cations, which indicate the presence of two domains in a 109° orientation relation.

The corresponding domain wall is marked with a red dashed line. The cross-section HAADF STEM image of BFO-BMN/LSMO/STO and corresponding EDS elemental mapping results are shown in Fig. 4(d). As expected, target elements of Ti, Mn, Fe, Bi, Mg, Nb, and Pt are distributed uniformly in the designed layers without obvious interfacial diffusion. The thicknesses of the BFO-BMN film and LSMO layer are identified to be 540 and 11 nm, respectively.

B. First-principles calculations

First-principles calculations are performed to explore the energetically stable structure and corresponding polarization after the incorporation of BMN into BFO. A $4 \times 4 \times 2$ supercell with 29 Fe, 2 Mg, and 1 Nb atoms on the *B* site is used. The space groups assumed for the supercells of bulk BFO-BMN and BFO are $P1$ and $R3c$, respectively. Here, 9.375-mol% BMN-substituted BFO is selected for simplicity, which is close to the composition in experiments. Possible configurations with different *B*-site atomic distributions are considered and shown in Figs. 5(a)–5(h) and Table S1 within the Supplemental Material [40]. It is found that the configuration with MgO_6 and NbO_6 octahedra connected end to end along the [010]

TABLE I. Comparison of the calculated structural parameters of BFO and BFO-BMN supercells.

Material	Strain	Lattice parameters							Ion displacement (\AA)	
		a (\AA)	b (\AA)	c (\AA)	α ($^\circ$)	β ($^\circ$)	γ ($^\circ$)	c/a	<i>A</i> site	<i>B</i> site
BFO	Relaxed	3.936	3.936	3.936	89.602	89.602	89.602	1.000	0.551	0.184
	Strained	3.905	3.905	3.954	89.634	89.634	89.602	1.013	0.546	0.177
BFO-BMN	Relaxed	3.942	3.944	3.945	89.575	89.574	89.579	1.001	0.574	0.205
	Strained	3.905	3.905	3.990	89.715	89.711	89.579	1.022	0.547	0.186

TABLE II. Calculated polarization of BFO and BFO-BMN supercells.

Material	Strain	Polarization ($\mu\text{C cm}^{-2}$)			
		$P_x/[100]$	$P_y/[010]$	$P_z/[001]$	P_s
BFO	Relaxed	52.5	52.5	52.5	90.9
	Strained	49.5	49.5	55.8	89.4
BFO-BMN	Relaxed	53.5	54.1	51.9	92.1
	Strained	50.4	51.4	59.0	93.1

direction is the most stable structure [Fig. 5(a)]. The linear arrangement of doped atoms is reasonable, taking into account the coulomb interactions between $\text{Mg}_{\text{Fe}}^{+}$ and $\text{Nb}_{\text{Fe}}^{+}$.

Both epitaxial BFO-BMN and BFO films exhibit some degrees of distortion from the bulk rhombohedral phase to a tetragonal-like structure due to in-plane compressive strains (Fig. 3). For comparison, structural parameters and ferroelectric polarizations are calculated for the fully relaxed (bulk) and fully strained states, as listed in Tables I and II, respectively. Bulk BFO-BMN has a larger lattice constant and stronger rhombohedral distortion than that of bulk BFO (Table I), causing a larger misfit strain than BFO during epitaxial deposition on LSMO/STO, and hence, higher elastic energy than BFO. In that case, a rotated

twinning structure tends to form in the BFO-BMN film to alleviate the constraints of the substrate, and thereby, partially relax the strain. Under the fully strained states, both BFO-BMN and BFO exhibit a structural change from a rhombohedral cell to a tetragonal-like one. The lattice of BFO-BMN is even closer to being tetragonal, with a smaller rhombohedral distortion and an increased c/a than BFO. These results are in agreement with those obtained from Fig. 3. As listed in Table II, the spontaneous polarization, P_s , along the [111] direction of bulk BFO-BMN is increased by about 1.3% compared with that of bulk BFO. The increase in intrinsic polarization is associated with the increase of A - and B -site ionic displacements. When compressive epitaxial strain is taken into account,

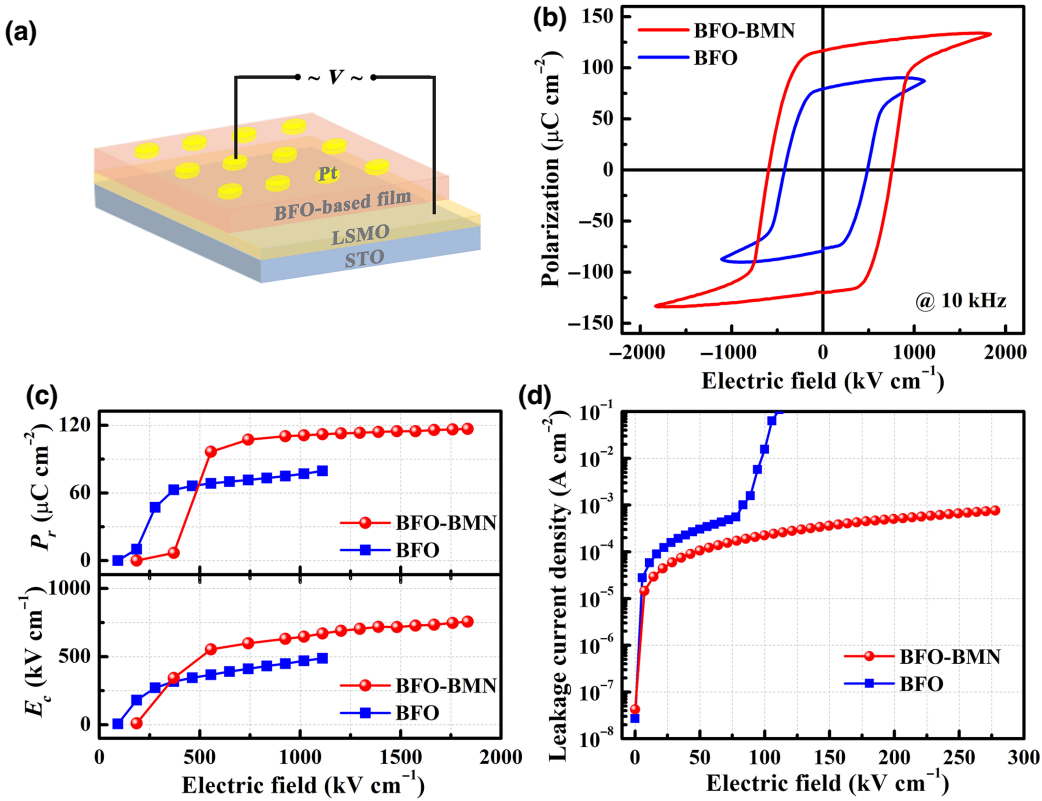


FIG. 6. (a) Schematic illustration of the BFO-based film capacitors for electrical measurements. (b) P - E hysteresis loops; (c) coercive field, E_c , and remanent polarization, P_r ; and (d) leakage current density as a function of electric field for epitaxial BFO-BMN and BFO films.

P_s usually shifts from the [111] direction toward the [001] direction, as a result of increased tetragonality, c/a , leading to an increase of out-of-plane polarization, P_z [57]. For both BFO and BFO-BMN, although the overall P_s remains almost the same, the in-plane compressive strain decreases the in-plane polarization, P_x and P_y , but increases the out-of-plane polarization, P_z . In particular, P_z is increased by about 13.7% in BFO-BMN, which is greater than 6.3% in BFO fully strained to the STO substrate. The introduction of BMN into BFO also leads to a 5.7% increase in P_z . Therefore, forming solid solutions with BMN is an effective way to enhance the remanent polarization of epitaxial (001) BFO films.

C. Electrical characterization

Electrical measurements are performed on the Pt/BFO-BMN/LSMO and Pt/BFO/LSMO capacitors, as schematically shown in Fig. 6(a). The P - E hysteresis loops of the epitaxial BFO-BMN and BFO films are shown in Fig. 6(b) and Fig. S7 within the Supplemental Material [40]. Corresponding coercive field, E_c , and remanent polarization, P_r , values of BFO-BMN and BFO as functions of electric field are shown in Fig. 6(c). Both films exhibit squarelike hysteresis loops. E_c and P_r increase with an increase of the applied external field until they saturate, as a result of more complete domain switching under a higher electric field. The larger E_c observed in the BFO-BMN film may be ascribed to disorder induced by substitution that is detrimental to domain-wall mobility [58,59]. The BFO-BMN film shows quite a large P_r of $116.8 \mu\text{C cm}^{-2}$, with a significant enhancement from that of the undoped BFO film ($P_r = 79.6 \mu\text{C cm}^{-2}$). The P_r value of the BFO-BMN film is comparable to that of supertetragonal ($c/a > 1.2$) BFO films ($P_r \sim 130\text{--}150 \mu\text{C cm}^{-2}$) [30,60], much larger than those of previously reported tetragonal-like epitaxial BFO ($P_r \sim 55 \mu\text{C cm}^{-2}$) [17] and Mn-doped BFO films ($P_r \sim 75 \mu\text{C cm}^{-2}$) [26]. This remarkably enhanced polarization in the BFO-BMN film can be attributed to the following three aspects: (i) first-principles calculations suggest that the introduction of BMN into BFO leads to a 5.7% increase in P_z under compressive strain; (ii) from the lattice parameters determined by the RSM measurements, the structure becomes more tetragonal-like with an increased tetragonality, c/a , after the addition of BMN; and (iii) the polarization extracted from in P - E measurements is actually the spontaneous polarization projected along the out-of-plane direction. The rotated twinning-domain structure results in an elongated projection onto the [001] direction, contributing to an increased P_r . In addition, the BFO-BMN film shows a leakage current density of $7.6 \times 10^{-4} \text{ A cm}^{-2}$, which is about 3 orders of magnitude lower than that of the pure BFO film, as shown in Fig. 6(d). The relatively low leakage current density is favorable for device applications.

IV. CONCLUSION

Epitaxial BFO-BMN and BFO films are deposited on (001)-oriented STO substrates with a LSMO buffer layer. Structural analyses show a unique rotated twinning-domain structure that develops in the BMN-modified BFO film, serving to partially relax epitaxial strain. By incorporating BMN, the lattice of the film becomes closer to a tetragonal structure, with an increased α from 89.72° to 89.91° , together with an increased tetragonality, c/a , from 1.018 to 1.037. The BFO-BMN film exhibits a large P_r of $116.8 \mu\text{C cm}^{-2}$, as a synergic effect of the increased intrinsic polarization, the increased tetragonality, and the rotated twinning domains upon incorporating BMN. These results demonstrate an effective composition-engineering strategy to optimize ferroelectric polarization.

ACKNOWLEDGMENTS

This work is supported by the National Key R&D Program of China (Grants No. 2022YFB3807603 and No. 2020YFA0711504) and the Natural Science Foundation of China (Grants No. 52232001, No. 52003117, and No. 11874207).

- [1] J. F. Scott, Applications of modern ferroelectrics, *Science* **315**, 954 (2007).
- [2] X.-K. Wei, N. Domingo, Y. Sun, N. Balke, R. E. Dunin-Borkowski, and J. Mayer, Progress on emerging ferroelectric materials for energy harvesting, storage and conversion, *Adv. Energy Mater.* **12**, 2201199 (2022).
- [3] S. He, M. F. Guo, Y. Wang, Y. H. Liang, and Y. Shen, An optical/ferroelectric multiplexing multidimensional non-volatile memory from ferroelectric polymer, *Adv. Mater.* **34**, 2202181 (2022).
- [4] L. Han, *et al.*, High-density switchable skyrmion-like polar nanodomains integrated on silicon, *Nature* **603**, 63 (2022).
- [5] W. Saenrang, *et al.*, Deterministic and robust room-temperature exchange coupling in monodomain multi-ferroic BiFeO₃ heterostructures, *Nat. Commun.* **8**, 1583 (2017).
- [6] F. Li, M. J. Cabral, B. Xu, Z. X. Cheng, E. C. Dickey, J. M. LeBeau, J. L. Wang, J. Luo, S. Taylor, W. Hackenberger, L. Bellaiche, Z. Xu, L.-Q. Chen, T. R. Shrout, and S. J. Zhang, Giant piezoelectricity of Sm-doped Pb(Mg_{1/3}Nb_{2/3})O₃-PbTiO₃ single crystals, *Science* **364**, 264 (2019).
- [7] M.-M. Yang, D. J. Kim, and M. Alexe, Flexo-photovoltaic effect, *Science* **360**, 904 (2018).
- [8] L. W. Martin, S. P. Crane, Y.-H. Chu, M. B. Holcomb, M. Gajek, M. Huijben, C.-H. Yang, N. Balke, and R. Ramesh, Multiferroics and magnetoelectrics: Thin films and nanostructures, *J. Phys.: Condens. Matter* **20**, 434220 (2008).
- [9] L. W. Martin and A. M. Rappe, Thin-film ferroelectric materials and their applications, *Nat. Rev. Mater.* **2**, 16087 (2017).

- [10] G. Wang, Z. L. Lu, Y. Li, L. H. Li, H. F. Ji, A. Feteira, D. Zhou, D. W. Wang, S. J. Zhang, and I. M. Reaney, Electroceramics for high-energy density capacitors: Current status and future perspectives, *Chem. Rev.* **121**, 6124 (2021).
- [11] R. Guo, L. You, Y. Zhou, Z. S. Lim, X. Zou, L. Chen, R. Ramesh, and J. L. Wang, Non-volatile memory based on the ferroelectric photovoltaic effect, *Nat. Commun.* **4**, 1990 (2013).
- [12] J. Y. Park, D.-H. Choe, D. H. Lee, G. T. Yu, K. Yang, S. H. Kim, G. H. Park, S.-G. Nam, H. J. Lee, S. Jo, B. J. Kuh, D. Ha, Y. Kim, J. Heo, and M. H. Park, Revival of ferroelectric memories based on emerging fluorite-structured ferroelectrics, *Adv. Mater.* **2204904** (2023).
- [13] T. Mikolajick, M. H. Park, L. Begon-Lours, and S. Slezacek, From ferroelectric material optimization to neuromorphic devices, *Adv. Mater.* **2206042** (2023).
- [14] Y. Yun, L. Kampschulte, M. Li, D. Liao, and E. I. Altman, Effect of ferroelectric poling on the adsorption of 2-propanol on $\text{LiNbO}_3(0001)$, *J. Phys. Chem. C* **111**, 13951 (2007).
- [15] A. Kakekhani and S. Ismail-Beigi, Ferroelectric-based catalysis: Switchable surface chemistry, *ACS Catal.* **5**, 4537 (2015).
- [16] G. Catalan and J. F. Scott, Physics and applications of bismuth ferrite, *Adv. Mater.* **21**, 2463 (2009).
- [17] J. Wang, J. B. Neaton, H. Zheng, V. Nagarajan, S. B. Ogale, B. Liu, D. Viehland, V. Vaithyanathan, D. G. Schlom, U. V. Waghmare, N. A. Spaldin, K. M. Rabe, M. Wuttig, and R. Ramesh, Epitaxial BiFeO_3 multiferroic thin film heterostructures, *Science* **299**, 1719 (2003).
- [18] D. X. Ji, S. H. Cai, T. R. Paudel, H. Y. Sun, C. C. Zhang, L. Han, Y. F. Wei, Y. P. Zang, M. Gu, Y. Zhang, W. P. Gao, H. X. Huyan, W. Guo, D. Wu, Z. B. Gu, E. Y. Tsymbal, P. Wang, Y. F. Nie, and X. Q. Pan, Freestanding crystalline oxide perovskites down to the monolayer limit, *Nature* **570**, 87 (2019).
- [19] P.-C. Wu, *et al.*, Twisted oxide lateral homostructures with conjunction tunability, *Nat. Commun.* **13**, 2565 (2022).
- [20] D. Sando, A. Barthélémy, and M. Bibes, BiFeO_3 epitaxial thin films and devices: Past, present and future, *J. Phys.: Condens. Matter* **26**, 473201 (2014).
- [21] L. Z. Li, Y. Zhang, L. Xie, J. R. Jokisaari, C. Beekman, J.-C. Yang, Y.-H. Chu, H. M. Christen, and X. Q. Pan, Atomic-scale mechanisms of defect-induced retention failure in ferroelectrics, *Nano Lett.* **17**, 3556 (2017).
- [22] F. Kubel and H. Schmid, Structure of a ferroelectric and ferroelastic monodomain crystal of the perovskite BiFeO_3 , *Acta Cryst. B* **46**, 698 (1990).
- [23] S. K. Streiffer, C. B. Parker, A. E. Romanov, M. J. Lefevre, L. Zhao, J. S. Speck, W. Pompe, C. M. Foster, and G. R. Bai, Domain patterns in epitaxial rhombohedral ferroelectric films. I. Geometry and experiments, *J. Appl. Phys.* **83**, 2742 (1998).
- [24] H. W. Jang, D. Ortiz, S.-H. Baek, C. M. Folkman, R. R. Das, P. Shafer, Y. B. Chen, C. T. Nelson, X. Q. Pan, R. Ramesh, and C.-B. Eom, Domain engineering for enhanced ferroelectric properties of epitaxial (001) BiFeO thin films, *Adv. Mater.* **21**, 817 (2009).
- [25] K.-E. Kim, S. Jeong, K. Chu, J. H. Lee, G.-Y. Kim, F. Xue, T. Y. Koo, L.-Q. Chen, S.-Y. Choi, R. Ramesh, and C.-H. Yang, Configurable topological textures in strain graded ferroelectric nanoplates, *Nat. Commun.* **9**, 403 (2018).
- [26] H. Béa, *et al.*, Evidence for Room-Temperature Multiferroicity in a Compound with a Giant Axial Ratio, *Phys. Rev. Lett.* **102**, 217603 (2009).
- [27] H. J. Liu, P. Yang, K. Yao, K. P. Ong, P. Wu, and J. Wang, Origin of a tetragonal BiFeO_3 phase with a giant c/a ratio on SrTiO_3 substrates, *Adv. Funct. Mater.* **22**, 937 (2012).
- [28] L. Xie, L. Z. Li, C. A. Heikes, Y. Zhang, Z. J. Hong, P. Gao, C. T. Nelson, F. Xue, E. Kioupakis, L. Q. Chen, D. G. Schlom, P. Wang, and X. Q. Pan, Giant ferroelectric polarization in ultrathin ferroelectrics via boundary-condition engineering, *Adv. Mater.* **29**, 1701475 (2017).
- [29] D. Kan, V. Anbusathaiah, and I. Takeuchi, Chemical substitution-induced ferroelectric polarization rotation in BiFeO_3 , *Adv. Mater.* **23**, 1765 (2011).
- [30] Z. Fan, J. X. Xiao, H. J. Liu, P. Yang, Q. Q. Ke, W. Ji, K. Yao, K. P. Ong, K. Y. Zeng, and J. Wang, Stable ferroelectric perovskite structure with giant axial ratio and polarization in epitaxial $\text{BiFe}_{0.6}\text{Ga}_{0.4}\text{O}_3$ thin films, *ACS Appl. Mater. Interfaces* **7**, 2648 (2015).
- [31] R. K. Shi, Y. P. Pu, W. Wang, X. Guo, J. W. Li, M. D. Yang, and S. Y. Zhou, A novel lead-free $\text{NaNbO}_3\text{-Bi}(\text{Zn}_{0.5}\text{Ti}_{0.5})\text{O}_3$ ceramics system for energy storage application with excellent stability, *J. Alloys Compd.* **815**, 152356 (2020).
- [32] Q. B. Yuan, G. Li, F.-Z. Yao, S.-D. Cheng, Y. F. Wang, R. Ma, S.-B. Mi, M. Gu, K. Wang, J.-F. Li, and H. Wang, Simultaneously achieved temperature-insensitive high energy density and efficiency in domain engineered $\text{BaTiO}_3\text{-Bi}(\text{Mg}_{0.5}\text{Zr}_{0.5})\text{O}_3$ lead-free relaxor ferroelectrics, *Nano Energy* **52**, 203 (2018).
- [33] P. Y. Zhao, H. X. Wang, L. W. Wu, L. L. Chen, Z. M. Cai, L. T. Li, and X. H. Wang, High-performance relaxor ferroelectric materials for energy storage applications, *Adv. Energy Mater.* **9**, 1803048 (2019).
- [34] X. L. Chen, J. Chen, D. D. Ma, L. Fang, and H. F. Zhou, Thermally stable $\text{BaTiO}_3\text{-Bi}(\text{Mg}_{2/3}\text{Nb}_{1/3})\text{O}_3$ solid solution with high relative permittivity in a broad temperature usage range, *J. Am. Ceram. Soc.* **98**, 804 (2015).
- [35] Z. L. Lu, G. Wang, W. C. Bao, J. L. Li, L. H. Li, A. Mostaed, H. J. Yang, H. F. Ji, D. J. Li, A. Feteira, F. F. Xu, D. C. Sinclair, D. W. Wang, S.-Y. Liu, and I. M. Reaney, Superior energy density through tailored dopant strategies in multilayer ceramic capacitors, *Energy Environ. Sci.* **13**, 2938 (2020).
- [36] G. Kresse and J. Furthmüller, Efficient iterative schemes for *ab initio* total-energy calculations using a plane-wave basis set, *Phys. Rev. B* **54**, 11169 (1996).
- [37] J. P. Perdew, K. Burke, and M. Ernzerhof, Generalized Gradient Approximation Made Simple, *Phys. Rev. Lett.* **77**, 3865 (1996).
- [38] K. Momma and F. Izumi, VESTA 3 for three-dimensional visualization of crystal, volumetric and morphology data, *J. Appl. Crystallogr.* **44**, 1272 (2011).
- [39] X. F. Wu, D. Vanderbilt, and D. R. Hamann, Systematic treatment of displacements, strains, and electric fields in density-functional perturbation theory, *Phys. Rev. B* **72**, 035105 (2005).

- [40] See the Supplemental Material at <http://link.aps.org/supplemental/10.1103/PhysRevApplied.19.054064> for more details of the structural and ferroelectric characterization and first-principles calculations.
- [41] F. Johann, A. Morelli, D. Biggemann, M. Arredondo, and I. Vrejoiu, Epitaxial strain and electric boundary condition effects on the structural and ferroelectric properties of BiFeO₃ films, *Phys. Rev. B* **84**, 094105 (2011).
- [42] Z. H. Chen, A. R. Damodaran, R. Xu, S. Lee, and L. W. Martin, Effect of “symmetry mismatch” on the domain structure of rhombohedral BiFeO₃ thin films, *Appl. Phys. Lett.* **104**, 182908 (2014).
- [43] Y. Q. Liu, Y. Wang, J. Ma, S. Li, H. Pan, C.-W. Nan, and Y.-H. Lin, Controllable electrical, magnetoelectric and optical properties of BiFeO₃ via domain engineering, *Prog. Mater. Sci.* **127**, 100943 (2022).
- [44] Z. H. Chen, Y. J. Qi, L. You, P. Yang, C. W. Huang, J. L. Wang, T. Sritharan, and Lang Chen, Large tensile-strain-induced monoclinic M_B phase in BiFeO₃ epitaxial thin films on a PrScO₃ substrate, *Phys. Rev. B* **88**, 054114 (2013).
- [45] C. J. M. Daumont, S. Farokhipoor, A. Ferri, J. C. Wojdeł, Jorge Íñiguez, B. J. Kooi, and B. Noheda, Tuning the atomic and domain structure of epitaxial films of multiferroic BiFeO₃, *Phys. Rev. B* **81**, 144115 (2010).
- [46] H. J. Liu, P. Yang, K. Yao, and J. Wang, Twinning rotation and ferroelectric behavior of epitaxial BiFeO₃(001) thin film, *Appl. Phys. Lett.* **96**, 012901 (2010).
- [47] A. Panchwanee, V. R. Reddy, R. J. Choudhary, D. M. Phase, V. Ganesan, and A. Gupta, Study of tilted orthorhombic twins and leakage current in epitaxial SmFeO₃ thin films, *J. Appl. Phys.* **125**, 234102 (2019).
- [48] A. Vailionis, H. Boschker, W. Siemons, E. P. Houwman, D. H. A. Blank, G. Rijnders, and G. Koster, Misfit strain accommodation in epitaxial ABO₃ perovskites: Lattice rotations and lattice modulations, *Phys. Rev. B* **83**, 064101 (2011).
- [49] H. J. Liu, K. Yao, P. Yang, Y. H. Du, Q. He, Y. L. Gu, X. L. Li, S. S. Wang, X. T. Zhou, and J. Wang, Thickness-dependent twinning evolution and ferroelectric behavior of epitaxial BiFeO₃(001) thin films, *Phys. Rev. B* **82**, 064108 (2010).
- [50] Y. J. Zhao, Z. G. Yin, X. W. Zhang, Z. Fu, and J. L. Wu, Formation and local conduction of nanopits in BiFeO₃ epitaxial films, *J. Mater. Chem. C* **3**, 11250 (2015).
- [51] José Santiso, L. Balcells, Z. Konstantinovic, J. Roqueta, P. Ferrer, A. Pomar, B. Martínez, and F. Sandiumenge, Thickness evolution of the twin structure and shear strain in LSMO films, *CrystEngComm* **15**, 3908 (2013).
- [52] Z. H. Chen, Z. L. Luo, Y. J. Qi, P. Yang, S. X. Wu, C. W. Huang, T. Wu, J. L. Wang, C. Gao, T. Sritharan, and L. Chen, Low symmetry monoclinic M_C phase in epitaxial BiFeO₃ thin films on LaSrAlO₄ substrates, *Appl. Phys. Lett.* **97**, 242903 (2010).
- [53] H. M. Christen, J. H. Nam, H. S. Kim, A. J. Hatt, and N. A. Spaldin, Stress-induced $R\text{-}M_A\text{-}M_C\text{-}T$ symmetry changes in BiFeO₃ films, *Phys. Rev. B* **83**, 144107 (2011).
- [54] M. Campanini, E. Gradauskaitė, M. Trassin, D. Yi, P. Yu, R. Ramesh, R. Erni, and M. D. Rossell, Imaging and quantification of charged domain walls in BiFeO₃, *Nanoscale* **12**, 9186 (2020).
- [55] C. T. Nelson, B. Winchester, Y. Zhang, S.-J. Kim, A. Melville, C. Adamo, C. M. Folkman, S.-H. Baek, C.-B. Eom, D. G. Schlom, L.-Q. Chen, and Xiaoqing Pan, Spontaneous vortex nanodomain arrays at ferroelectric heterointerfaces, *Nano Lett.* **11**, 828 (2011).
- [56] Y. L. Tang, Y. L. Zhu, X. L. Ma, A. Y. Borisevich, A. N. Morozovska, E. A. Eliseev, W. Y. Wang, Y. J. Wang, Y. B. Xu, Z. D. Zhang, and S. J. Pennycook, Observation of a periodic array of flux-closure quadrants in strained ferroelectric PbTiO₃ films, *Science* **348**, 547 (2015).
- [57] H. W. Jang, S. H. Baek, D. Ortiz, C. M. Folkman, R. R. Das, Y. H. Chu, P. Shafer, J. X. Zhang, S. Choudhury, V. Vaithyanathan, Y. B. Chen, D. A. Felker, M. D. Biegalski, M. S. Rzchowski, X. Q. Pan, D. G. Schlom, L. Q. Chen, R. Ramesh, and C. B. Eom, Strain-Induced Polarization Rotation in Epitaxial (001) BiFeO₃ Thin Films, *Phys. Rev. Lett.* **101**, 107602 (2008).
- [58] P. Paruch, T. Giamarchi, and J.-M. Triscone, Domain Wall Roughness in Epitaxial Ferroelectric PbZr_{0.2}Ti_{0.8}O₃ Thin Films, *Phys. Rev. Lett.* **94**, 197601 (2005).
- [59] Y. Feng, J. G. Wu, Q. G. Chi, W. L. Li, Y. Yu, and W. D. Fei, Defects and aliovalent doping engineering in electroceramics, *Chem. Rev.* **120**, 1710 (2020).
- [60] J. X. Zhang, Q. He, M. Trassin, W. Luo, D. Yi, M. D. Rossell, P. Yu, L. You, C. H. Wang, C. Y. Kuo, J. T. Heron, Z. Hu, R. J. Zeches, H. J. Lin, A. Tanaka, C. T. Chen, L. H. Tjeng, Y.-H. Chu, and R. Ramesh, Microscopic Origin of the Giant Ferroelectric Polarization in Tetragonal-like BiFeO₃, *Phys. Rev. Lett.* **107**, 147602 (2011).